ADVANCED FUNCTIONAL MATERIALS
www.afm-journal.de

Electrochemically Driven Tandem In-Plane Reduction and $FeCl_3$- Intercalation of Highly Crystalline Graphene Oxide Thin Films

Tatsuki Tsugawa, Kazuto Hatakeyama, Junya Kawasaki, Agamoni Pathak, Kazuhito Tsukagoshi, Shintaro Ida,* and Takaaki Taniguchi**

The current design and understanding of graphene oxide (GO) and reduced GO (rGO) materials rely largely on insights derived from structurally defective and chemically inhomogeneous GO synthesized by Hummers' method. As a result, this early-stage knowledge fails to fully exploit the potential benefits of GO. This study explores electrochemical approaches using highly crystalline Brodie's GO for fabricating reduced GO (rGO)-based transparent conductive films (TCFs) without using toxic reducing agents or heat treatment.

The study first demonstrates an in-plane electrochemical reduction method for fabricating rGO nanocoatings on plastic substrates. During this process, rGO at the rGO/GO/electrolyte three-phase interface functions as a growing cathode, inducing tandem reduction parallel to the insulating substrate surface. The crystallinity of the GO precursor determines the activation or deactivation of the three-phase interface at nanometer-scale thickness. The electrochemical reduction of epoxide groups leads to a well-extended π-electron network with suppressed local strains and carbon vacancies. The sheet resistivity of rGO-based TCFs is further optimized through hole doping via electrochemical $FeCl_3$ intercalation, breaking the transparency–resistivity limit of available rGO-TCFs. These discoveries will facilitate the development of next-generation green graphene processes based on precise synthetic chemistry.

1. Introduction

Graphene has remarkable structural flexibility, good chemical stability, high electrical and thermal conductivity, and uniform optical transmission from visible to near-infrared wavelengths.[1–5] These characteristics provide opportunities to develop ultrathin devices in a wide range of technical fields, from nanoelectronics to industrial coatings. Chemical vapor deposition (CVD) has proven most effective for producing graphene thin films, allowing precise control over domain size, layer numbers, and carrier transport properties.[6–10] However, CVD presents considerable drawbacks, including high costs, substantial energy consumption, and process toxicity. Moreover, the complex transfer process required to move graphene layers from Cu or Ni growth substrates to target substrates presents further challenges, limiting widespread practical applications.[11,12]

The reduction of graphene oxide (GO), synthesizable in large quantities from natural graphite, represents a viable approach for industrial graphene production. Since Ruoff et al. demonstrated the chemical reduction of GO using hydrazine,[13] numerous reduction techniques have emerged,[14,15] leveraging chemical and thermal driving forces both independently and in combination. These developments have also simultaneously highlighted specific critical technical challenges in GO-to-graphene conversion.[16,17] First, although chemical reduction initiates at a low temperature, conventional reducing agents such as $NaBH_4$,[18] hydriodic acid,[19] and liquid ammonia[20] exhibit high toxicity and reactivity.[21,22] Moreover, the limited deoxygenation capability of chemical reduction necessitates additional heat treatment during or after the reaction to achieve high conductivity.[23] This thermal deoxygenation, however, generates CO and CO_2 gases, creating carbon vacancies that reduce carrier mobility.[24] High-temperature reduction at least above 1000 °C is required to repair the atomic vacancies.[13] Addressing these limitations often necessitates the use of sophisticated, expensive equipment like laser and microwave irradiation systems,[25–30] which negate the industrial advantages of GO processing. Another significant challenge arises from the

T. Tsugawa, J. Kawasaki
Graduate School of Science and Technology
Kumamoto University
Kumamoto 850-8555, Japan
K. Hatakeyama, S. Ida
Institute of Industrial Nanomaterials (IINa)
Kumamoto University
Kumamoto 860-8555, Japan
E-mail: hatakeyama-k@kumamoto-u.ac.jp; ida-s@kumamoto-u.ac.jp
A. Pathak, K. Tsukagoshi, T. Taniguchi
Research Center for Materials Nanoarchitectonics (MANA)
National Institute for Materials Science (NIMS)
Tsukuba 305-0044, Japan
E-mail: taniguchi.takaaki@nims.go.jp

The ORCID identification number(s) for the author(s) of this article can be found under https://doi.org/10.1002/adfm.202510430

DOI: 10.1002/adfm.202510430

poor crystallinity of pristine GO, particularly when synthesized using the Hummers' method—the most widely adopted GO synthesis technique.[31,32] This method introduces substantial structural and compositional disorders in the two-dimensional GO lattice,[31] degrading the carrier transport properties of individual reduced GO (rGO) nanosheets. Therefore, although GO-related research has increasingly shifted toward practical applications, we still need a deeper insight into the chemistry of GO, including oxidation mechanisms[33–35] and chemical reactivity[36–41] in order to pursue the green production of graphene-based functional nanomaterials.

Recently, we demonstrated an electrochemical reduction mechanism for GO proceeding through the following two reactions in an aqueous solution at room temperature, as evidenced by the monitoring of functional groups and carbon radicals during repeated electrochemical oxidation–reduction cycles.[42]

$$C-O-C + 2e^- + 2H^+ \rightarrow C=C + H_2O \quad (1)$$

$$C-O-C + 2e^- + 2H^+ \rightarrow C-OH + C-H \quad (2)$$

Notably, this mechanism enables reduction without generating carbon vacancies. Furthermore, in-plane X-ray diffraction analysis revealed that GO synthesized using Brodie's method (B-GO) exhibits superior uniformity in chemical composition and higher crystallinity compared to GO synthesized using Hummers' method (H-GO),[31] establishing B-GO as a preferred precursor for low-temperature thermal reduction at 300 °C. In addition, individual B-GO nanosheets are virtually free of nanopores normally found in H-GO nanosheets,[43] as recently demonstrated by vertical proton blocking properties of B-GO membranes.[44] Therefore, although both H-GO and B-GO are commonly referred to as GO, they should be recognized as distinct materials due to their largely different crystallinities and physical properties. Building on these findings, the present study aims to explore a greener electrochemical reduction process for rGO-based transparent conductive films (TCFs) without toxic chemical additives or heat treatment. The results demonstrate successful fabrication of rGO-based TCFs directly on insulating substrates through tandem in-plane electrochemical reduction at a three-phase interface comprising growing rGO (cathode), unreduced GO (reactant), and an electrolyte. The efficacy of this process depends on the use of B-GO; substitution with H-GO significantly inhibits the tandem reduction at the three-phase interface, resulting in poorly conductive rGO thin films because of defective rGO cathode formation.

Further, intercalation chemistry is utilized to reduce the resistivity of rGO thin films. The interlayer spacing of graphite allows the intercalation of various molecules and ions, forming graphite intercalation compounds with distinct electrical and magnetic properties compared to pristine graphite. Specifically, the intercalation of metal chlorides, such as $FeCl_3$, $AuCl_3$, and $MoCl_5$, has been demonstrated to effectively modulate the electrical properties of bilayer and few-layer graphene.[45–47] However, chloride intercalation in rGO layers stacked without specific in-plane crystallographic orientation remains unexplored. This study demonstrates conductivity enhancement through hole doping via room-temperature electrochemical $FeCl_3$ intercalation, establishing an interface chemistry approach for refining GO-based nanomaterials. Additionally, optimization of GO film quality through spin coating results in further resistivity reduction at transparency levels exceeding 90%, yielding figures of merit that surpass corresponding values for previously reported rGO-based TCFs. The environmentally friendly electrochemical approach and deepened GO chemistry offer potential for functionalizing and industrializing diverse GO and rGO-based nanomaterials.

2. Results and Discussion

2.1. In-plane Electrochemical Reduction of GO Thin Films

Figure 1a,b illustrates the electrochemical reduction mechanisms of GO films on conductive and insulating substrates, respectively. On conductive substrates, electrons transfer from the substrate surface to the adjacent GO layer. The electrolyte diffused into the interfaces between GO layers provides protons for electrochemical reduction Equations (1) and (2). The freshly formed rGO layer functions as a cathode at the rGO/GO/electrolyte three-phase interface, promoting reduction perpendicular to the surface—a process designated as the through-plane reduction mode. Meanwhile, on insulating substrates, a conductive material in contact with part of the GO film acts as a cathode and initiates reduction. Similar to the conductive substrate case, the three-phase interface sequentially develops under applied bias; however, the rGO region expands parallel to the substrate surface, a process termed as the in-plane reduction mode. Among the numerous studies on GO electrochemical reduction, to our knowledge, only two have investigated in-plane reduction. The first study demonstrated effective in-plane reduction in 7-μm-thick H-GO films, achieving a conductivity of ≈8.50×10^3 S m^{-1}.[48] Meanwhile, the second study showed that the reduction of nanoscale-thickness H-GO thin films resulted in electrical resistivities as high as 1–3 kΩ m^{-1}, 10^8 times higher than that of commercial ITO substrates.[49] This observation indicates a nanoscale effect inhibiting in-plane reduction in thin films. We hypothesize that the nanoscale thickness of the rGO cathode potentially limits electron supply to reduction sites, resulting in incomplete reduction. If this is true, an effective solution would involve substituting conventional H-GO with highly crystalline B-GO, as the enhanced electrical conductivity of reduced B-GO may facilitate nanoscale cathode activation.

The atomic force microscopy (AFM) image in Figure 1c reveals that the monolayer B-GO nanosheets used in this study have an average thickness of ≈1 nm and a lateral sheet size of ≈ 2–5 μm (Figure S1, Supporting Information). These nanosheets were deposited on polyethylene terephthalate (PET) substrates using layer-by-layer (LbL) assembly to fabricate GO thin films. The process began with surface modification of the substrate by depositing a polycationic layer of poly(diallyldimethylammonium chloride) (PDDA) to impart positive charge, followed by its immersion in a B-GO dispersion to allow negatively charged B-GO nanosheets to attach electrostatically. Figure 1d illustrates the reduction of a five-cycle LbL-processed B-GO film at −1.7 V (vs Ag/AgCl) in a 0.005 M H_2SO_4 electrolyte. The reduction process initiated at the glassy carbon (GC)/GO/electrolyte interface, with the darker-colored rGO region expanding laterally over time. Prolonging the reduction time by 2400 s resulted in

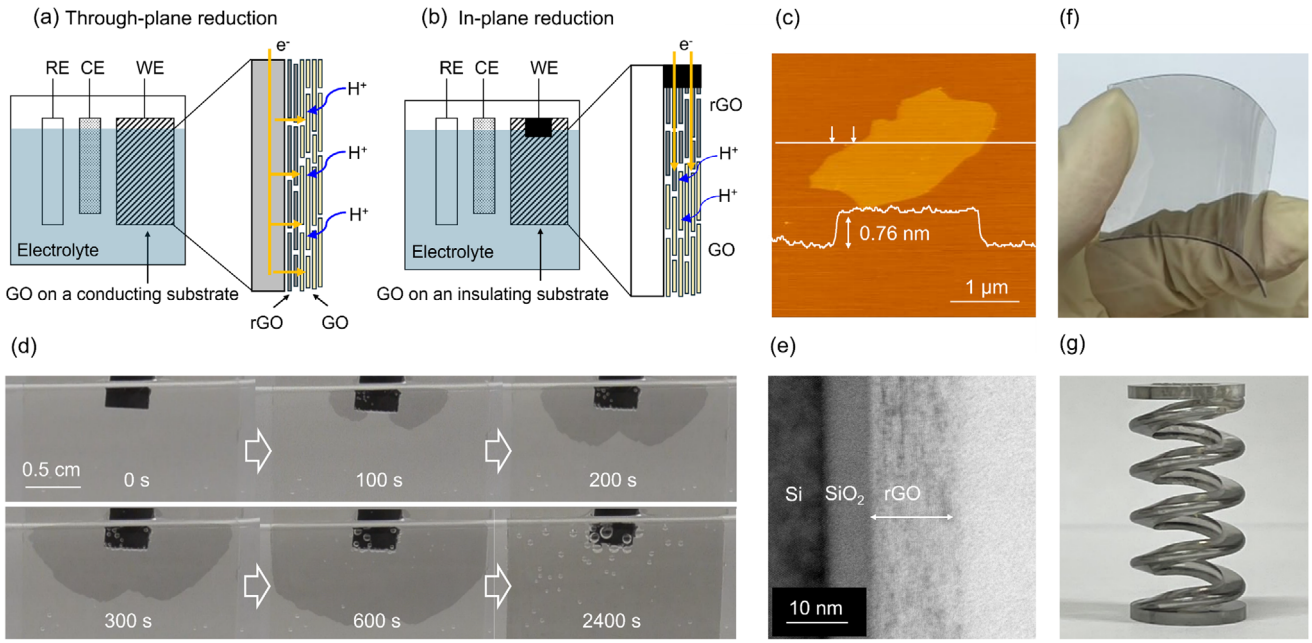

Figure 1. Schematics illustrating (a) the through-plane electrochemical reduction of a GO film on a conducting substrate and (b) the in-plane electrochemical reduction of a GO film on an insulating substrate. c) AFM image of B-GO nanosheets. d) Snapshots of the electrochemical in-plane reduction of a five-cycle LbL-deposited B-GO film on a PET substrate. The corresponding movie is available in Figure S1 (Supporting Information). e) Cross-sectional TEM image of a five-cycle LbL-deposited rGO film. For this observation, an SiO_2/Si substrate was used to facilitate specimen fabrication via focused ion beam processing. rGO films formed (f) flexible and (g) spring-shaped PET substrates. The diameter of the spring is 1 cm.

the resistivity to 1.6 kΩ sq^{-1}. The resistivity of the electrochemically reduced B-GO film surpassed that of a B-GO film prepared under the same LbL deposition conditions but subjected to high-temperature thermal reduction at 700 °C under an H_2/Ar gas flow (2 kΩ sq^{-1}).[31] Electrochemical reduction therefore represents an effective process for converting GO to highly conductive rGO at room temperature without using hazardous chemicals or forming byproducts. Cross-sectional transmission electron microscopy (TEM) observation revealed an ≈15-nm-thick rGO film under the current deposition and reduction conditions (Figure 1e). An rGO coating on a flexible PET substrate, prepared under the same deposition and reduction conditions, formed a bendable conducting sheet (Figure 1f). Furthermore, the proposed electrochemical reduction process enables conductive coating on complex-shaped substrates—a feature difficult to achieve with conventional CVD graphene processes. For example, GO deposited on a plastic spring underwent uniform reduction to form a continuous rGO layer (Figure 1g), enabling LED illumination upon bias voltage application to the spring ends (Figure S2, Supporting Information).

As a control experiment, electrochemical reduction was performed using H-GO, instead of B-GO. However, the reduction of the H-GO film remained localized around the GC contact area throughout the reaction duration (2400 s) (Figure S3, Supporting Information). Furthermore, the resistivity of the reduced area ranged from 59–145 MΩ sq^{-1}, ≈10^8 times higher than that of the reference ITO substrate (10 Ω sq^{-1}). Notably, five-cycle LbL deposition of B-GO and H-GO should yield similar film thicknesses.[31] Therefore, differences in thickness can be ruled out as a factor contributing to deactivation of the rGO/GO/electrolyte interface. In our previous study, we demonstrated that the in-plane proton conductivity of pristine H-GO (2.9 × 10^{-3} S cm^{-1} at 100% RH) is an order of magnitude higher than that of pristine B-GO.[44] Therefore, the supply of H^+ across the trilayer interface is unlikely to be the rate-limiting factor in the strongly suppressed reduction of H-GO. In addition, we found that B-GO could achieve a low resistivity of 4 kΩsq^{-1} through thermal reduction at 300 °C, whereas H-GO reduced under the same conditions exhibited a ≈20-fold higher resistivity.[31] This significant resistivity difference suggests that a higher activation energy is required either to mitigate structural disorder in H-GO and to promote the proposed in-plane reduction reactions. Consequently, the three-phase interface could deactivate at defective 1D rGO/GO boundaries. These findings demonstrate that the use of B-GO or highly crystalline GO is essential for fabricating rGO-based TCFs via electrochemical reduction, as their crystallinity profoundly influences not only physical properties but also chemical reactivity.

2.2. Characterization of rGO-Based TCFs Obtained via Electrochemical Reduction

X-ray photoelectron spectroscopy (XPS) was performed to investigate the carbon bonding states before and after electrochemical reduction at −1.7 V (vs Ag/AgCl) in a 0.005 M H_2SO_4 electrolyte. As illustrated in the C 1s XPS spectra in **Figure 2a**, pristine GO displayed two primary peaks corresponding to carbon–carbon (C—C) and epoxy (C—O—C) bonds at 285 and 287.1 eV, respectively.[44,50] Upon reduction, the epoxy peak nearly

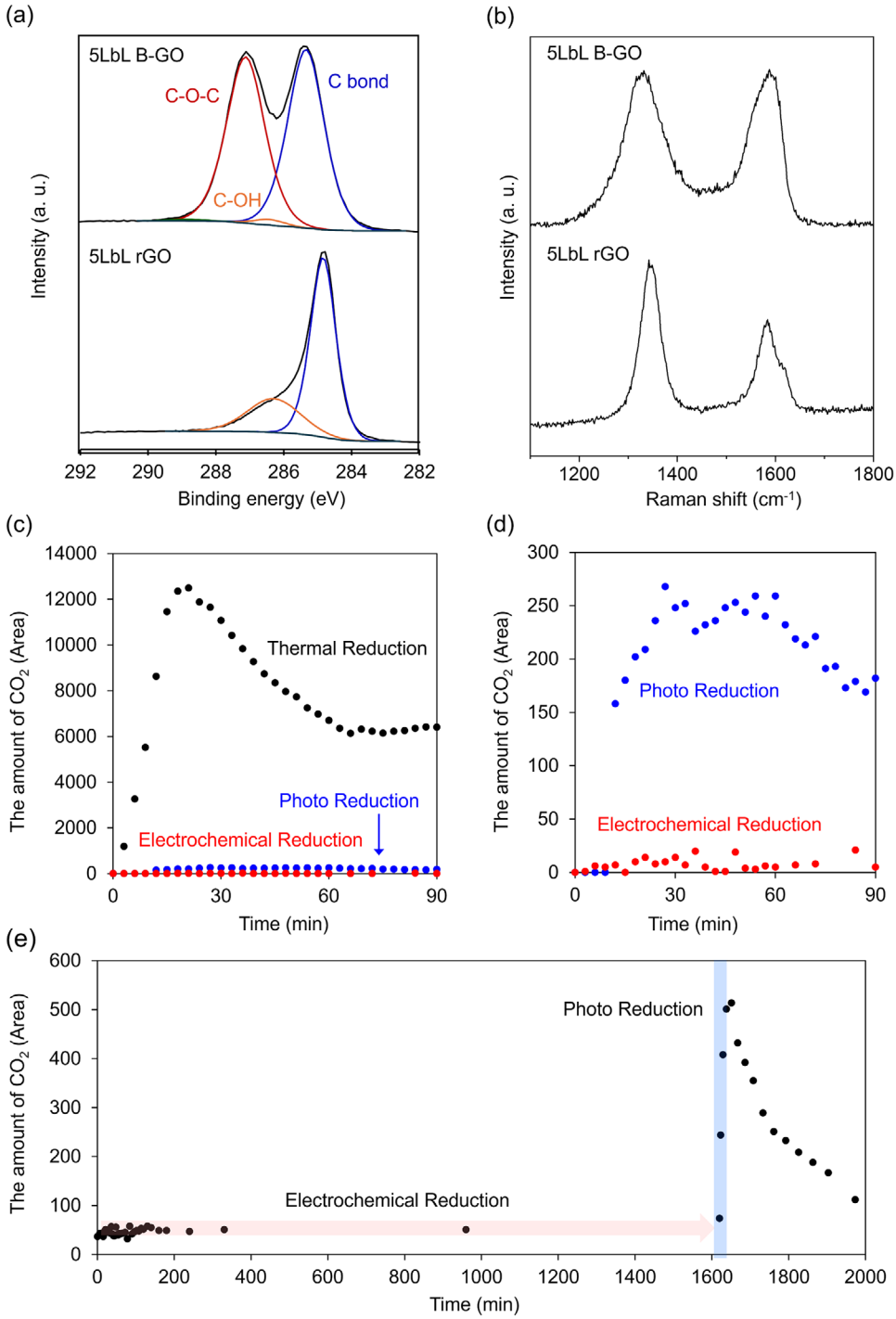

Figure 2. a) C 1s XPS spectra and b) Raman spectra of pristine and electrochemically reduced B-GO films deposited via five-cycle LbL assembly on quartz glass. c,d) In situ detection of CO_2 during thermal, photoinduced, and electrochemical reduction, presented with different Y-axis scales. d) In situ detection of CO_2 evolved during electrochemical reduction followed by photoinduced reduction.

disappeared, while the C—C peak intensified owing to the formation of C═C bonds, as described by Equation (1). Additionally, the relative intensity of the peak corresponding to the C—OH bond increased compared to that of the C—C peak, suggesting that Equation (2), which involves the formation of C—OH bonds (286.4 eV), possibly accompanied by C—H bond formation, should be considered. Figure 2b presents the Raman spectra of these samples. Before reduction, broad D and G bands with half-maximum full-width (HMFWH) values of 114 and 122 cm^{-1} were detected at 1332 and 1588 cm^{-1}, respectively. After reduction, both peaks narrowed to FWHM values of 32 and 52 cm^{-1}, respectively, while the strong D band was retained. The thermal

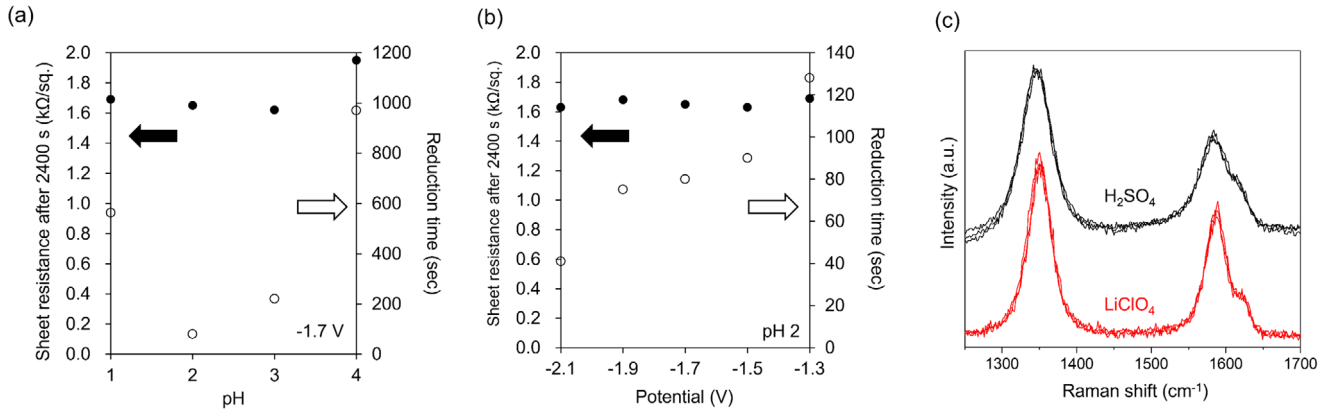

Figure 3. a) In-plane electrochemical reduction time and resulting sheet resistivity of 1 cm × 2.5 cm in size B-GO films deposited via five-cycle LbL assembly on a PET substrate, plotted as functions of (a) pH and (b) applied potential. c) Raman spectra of a five-cycle LbL-deposited rGO film electrochemically reduced in 0.005 M H_2SO_4/water and 1 M $LiClO_4$/acetonitrile electrolytes. The spectra measured on three different positions are displayed for each sample. These samples were deposited on quartz substrate.

reduction of B-GO by 700 °C in our previous study largely preserved the width of the G and D bands,[31] highlighting a structural distinction between thermally and electrochemically reduced B-GO.

To acquire reliable insights from the Raman spectra, the gases produced during thermal, photo-, and electrochemical reduction were analyzed using gas chromatography. As depicted in Figure 2c,d, CO_2 was detected immediately after the start of heat treatment to 300 °C for thermal reduction, indicating that oxygen atoms in the GO lattice were removed along with carbon atoms as CO_2. While photoreduction also generated CO_2, the detected amount was approximately 50 times lower than that observed during thermal reduction. In contrast, the amount of CO_2 evolved during electrochemical reduction was close to the detection limit. However, CO_2 was detected immediately after switching the reduction method from electrochemical to photoreduction (Figure 2e), confirming that CO_2 generated in the electrolyte was detectable using the experimental setup. These results suggest that electrochemical GO reduction proceeds with minimal CO_2 formation and carbon vacancy generation.

Based on the presence and absence of carbon vacancy formation in the thermal and electrochemical reduction of B-GO, respectively, as revealed by the analysis of evolved gas, the Raman spectra can be interpreted as follows. First, the D band in pristine B-GO is activated owing to phonon confinement by abundant epoxy groups. The epoxy-bridged C—C bond expands, inducing local lattice distortion, which broadens the G and D bands. The persistence of a strong D band after electrochemical reduction suggests phonon confinement by C—OH and C—H bonds, mirroring the effect of epoxide groups. However, these bonds create less pronounced lattice distortion in the graphene framework compared to the original epoxy-modified B-GO structure, explaining the observed sharpening of the G and D bands. In contrast, the persistent broad G and D bands observed after the thermal reduction of B-GO indicate that the relaxation of local lattice distortion following epoxide removal is counterbalanced by new distortions originating from carbon vacancy formation.[31] This interpretation of Raman spectra provides broader insights into the structure and properties of GO-related materials beyond the characterization of rGO obtained via the electrochemical reduction of B-GO.

2.3. Kinetic Control of Electrochemical Reduction Reactions

The above characterizations indicate that electrochemical reduction proceeds primarily through reactions (1) and (2), with reaction kinetics expected to depend on proton concentration. To examine this dependence, we conducted electrochemical reduction experiments in 0.05, 0.005, 0.0005, and 0.00005 M H_2SO_4 electrolytes at pH 1, 2, 3, and 4, respectively. The results confirmed that reduction kinetics generally accelerated as pH dropped (**Figure 3a**), while observed vigorous H_2 evolution was likely associated with the slowed reduction rate at pH 1. Additionally, at pH 2, the reduction reaction was accelerated at a negative reduction potential of −1.3 to −2.1 V (vs Ag/AgCl) (Figure 3b). These findings are generally consistent with those reported by Quezada-Renteria et al. for the pH- and bias-driven electrochemical through-plane reduction of H-GO.[51] However, no linear correlation was observed between the reduction rate and electrical resistance in our experiments, where resistances were ≈ 1.6 kΩ sq^{-1}. Thus, while lowering pH or applying a more negative potential accelerates the overall reaction rates of Equations (1) and (2), Equation (1), which extends the π-conjugated network, is not selectively promoted. As an alternative approach, electrochemical reduction was performed in a nonaqueous electrolyte consisting of 1 M $LiClO_4$ dissolved in acetonitrile. As a result, applying a bias voltage of −4 V induced the formation of a three-phase interface, yielding an rGO film with improved resistivity of 0.712 kΩ sq^{-1}. In the Raman spectra (Figure 3c), the G and D bands became sharper after reduction, mirroring the trend observed for rGO electrochemically reduced in an aqueous electrolyte. Simultaneously, the relative intensity of the G band to the D band increased, suggesting that the observed resistivity decrease was associated with the more extended sp^2 carbon network owing to the enhanced reaction rate of (1).

Based on our current findings and previous study on the thermal reduction of B-GO and H-GO, we have clarified the critical role of in-plane crystallinity in electronic transport. First, thermally reduced B-GO exhibits higher conductivity than thermally reduced H-GO due to its initially lower carbon vacancy density. Then, electrochemical reduction of B-GO in H_2SO_4 results in higher conductivity than thermally reduced rGO, as carbon vacancy formation during deoxygenation is suppressed. Electrochemical reduction in non-aqueous electrolytes further enhances conductivity by promoting the restoration of conjugated C═C bonds and suppressing the formation of C—OH groups potentially acting as electron scatters. In addition, electrochemically reduced B-GO in the non-aqueous system clearly exhibits superior conductivity compared to B-GO thermally reduced at 700 °C, where interlayer species could be thermally removed. This suggests that in-plane transport exerts a greater influence on the electrical conductivity of the rGO films than interlayer transport. Note that in-plane reduction in the non-aqueous electrolyte was slow, requiring ≈5000 s to fully reduce the GO layer deposited on a 1 cm × 2.5 cm quartz substrate. Additionally, PET was dissolved in acetonitrile, rendering the non-aqueous approach unsuitable for fabricating rGO-based TCFs on plastic substrates. Therefore, we tentatively selected the aqueous electrolyte system. Subsequent experiments were conducted under pH 2 and a reduction potential of −1.7 V as optimal conditions balancing reduction rate with resistivity based on the experimental results.

2.4. Electrochemical FeCl3 Intercalation into rGO-Based TCFs

The interfacial modification of thin films prepared by the deposition of chemically exfoliated nanosheets has traditionally focused on removing or reducing impurities between nanosheets.[52,53] Unlike such passive approaches, this study introduces an active intercalation strategy to lower the resistivity of rGO-based TCFs. Among the various functional intercalants used for graphene layers prepared via mechanical exfoliation and CVD growth, $FeCl_3$, which induces p-type doping, is widely employed owing to its availability, stability, and ease of handling.[45,46] Although $FeCl_3$ intercalation has been previously achieved through thermal reactions at 300–360 °C, it can also be electrochemically intercalated into bulk graphite at room temperature.[54] In this study, an electrochemical approach was adopted, as it enables the direct fabrication of rGO-based TCFs on substrates with low heat resistance. The intercalation conditions namely the application of a constant potential of +1.7 V (vs Ag/AgCl) for 400 s in a 9 M $FeCl_3$ aqueous solution—were based on previously examined $FeCl_3$ intercalation in bulk graphite. Consequently, the sheet resistivity of the rGO film obtained via five-cycle LbL deposition decreased by ≈70% to 458.4 Ω sq^{-1}. The rate of resistivity reduction was comparable to that achieved via thermal $FeCl_3$ intercalation in CVD-grown bilayer graphene films.[47] The sheet resistivity remained stable at this value for over six months under ambient conditions. In subsequent durability tests conducted at the thermal tolerance limit of PET (60 °C) under high humidity (90% RH), no significant degradation in sheet resistance (≈ 6%) was observed over a period of 240 h (Figure S4, Supporting Information), although the PET substrate exhibited slight bending. The robustness of $FeCl_3$-intercalated rGO under these conditions is in good agreement with the excellent environmental durability reported for thermally $FeCl_3$-intercalated few-layer graphene by Wehenkel et al.[55] Cross-sectional elemental mapping using TEM–energy-dispersive X-ray (EDX) spectroscopy confirmed the uniform distribution of Fe and Cl species throughout the rGO film (**Figure 4a**). Furthermore, high-resolution imaging revealed lattice fringes corresponding to the interlayer spacing of rGO, with no observable particulate impurities (Figure 4b). Electron energy loss spectroscopy (EELS) on the film revealed Fe $L_{2,3}$ edges consisting of the two peaks of Fe^{3+} species (Figure 4c).[56] These results suggest that $FeCl_3$ molecules not only adsorbed onto the surface but also diffused into the layered structure. The C 1s XPS spectra showed two peaks from C—C and C—OH bonds (Figure 4d), excluding the electrochemical oxidation of rGO during the anodic intercalation reaction. The Fe 2p XPS spectra supported a predominant trivalent iron state, where Cl/Fe and Fe/C elemental ratios were 2.08 and 0.026, respectively (Figure 4e). The Cl/Fe ratio of less than three suggests that a fraction of Fe^{3+} ions formed compounds other than $FeCl_3$. Moreover, the Fe/C ratio was lower than that obtained for electrochemically $FeCl_3$-intercalated bulk graphite (0.05–0.1). Accordingly, we suggest that the disordered interlayer structure of rGO, characterized by random in-plane orientation and residual hydroxyl groups, acts as a steric barrier to $FeCl_3$ insertion during electrochemical intercalation. Raman spectroscopy showed a slight shift in the D and G band to higher frequencies, ≈ 5 cm^{-1}, following electrochemical $FeCl_3$ intercalation (Figure 4f). This shift indicates that $FeCl_3$ intercalation induced hole doping,[46,57] contributing to the resistivity reduction of the rGO film. In the referenced study, electrochemical $FeCl_3$ intercalation in bulk graphite gradually reduced the intensity of the original G band at ≈1580 cm^{-1}, while an additional G band appeared at ≈1620 cm^{-1}.[54] Only the latter band is observed when the interlayer space is fully occupied with $FeCl_3$. In our case, the 1620 cm^{-1} band was not detected, likely due to the lower intercalation level, as confirmed by XPS analysis. Nevertheless, previous studies have shown that pristine graphene subjected to thermal $FeCl_3$ intercalation exhibited an efficient reduction in sheet resistance even at low intercalation levels with G band shift of 10 cm^{-1},[58] while further doping did not lead to significant additional improvements. This behavior suggests that intercalants not only act as p-type dopants to increase carrier concentration but also degrade carrier mobility due to enhanced scattering. Thereofore, even a modest degree of $FeCl_3$ intercalation, as achieved in the present study, was sufficient to induce a reduction in sheet resistivity. Although challenges remain in precisely controlling the location and density of the intercalated species, these results demonstrate the successful intercalation of metal chlorides into rGO layers that are stacked without preferential orientation to improve TCF performance.

2.5. Transparency and Resistivity Relationship

To examine the correlation between optical transmittance and electrical resistivity, rGO films with and without $FeCl_3$ intercalation were additionally prepared using 1–4 cycles of LbL deposition. As illustrated in **Figure 5a**, the transparency of the films increased progressively as the number of deposition cycles decreased. The plot of optical transmittance at 550 nm (T550 (%))

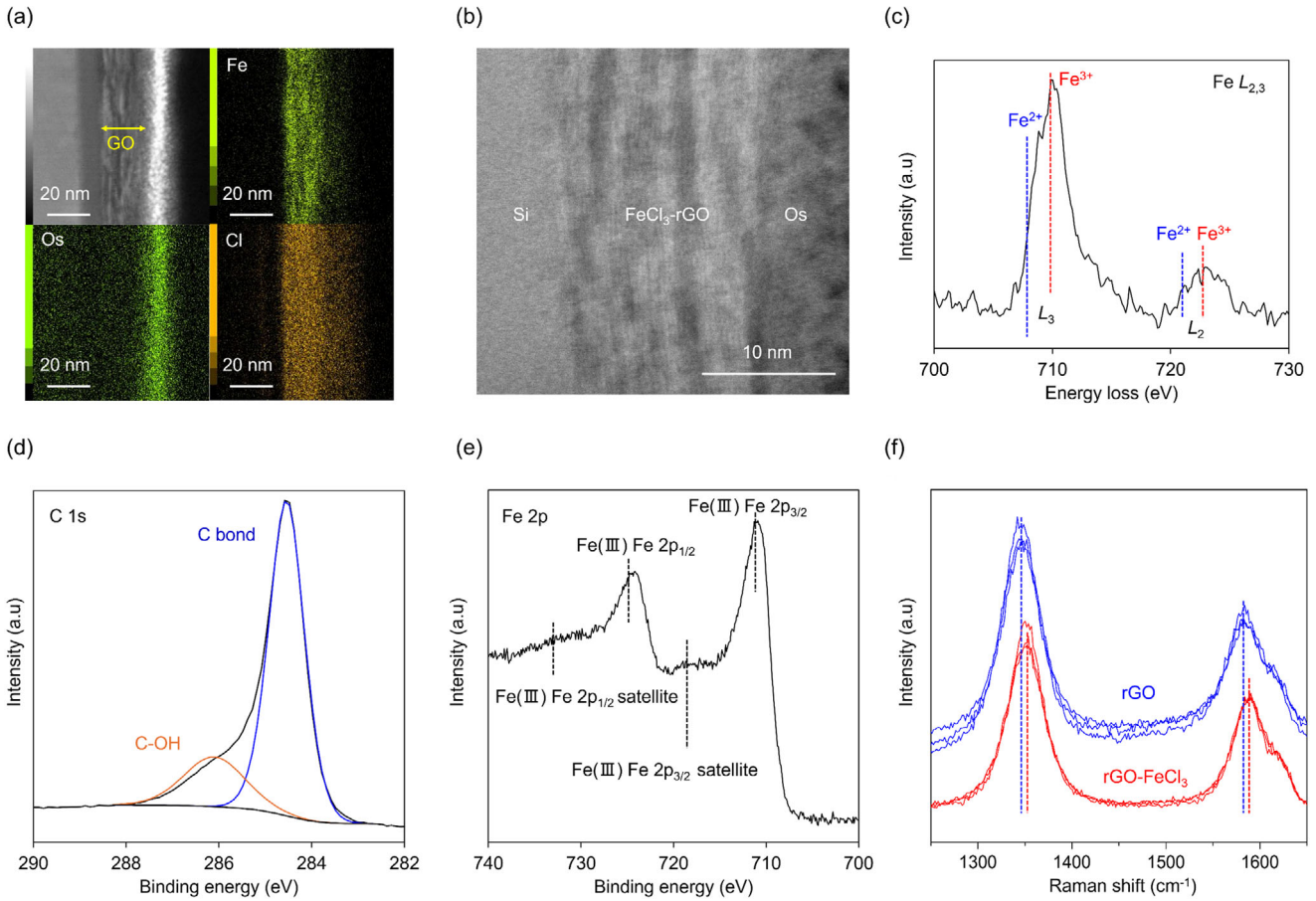

Figure 4. a) Cross-sectional images with EDX elemental mapping, and b) high magnification image, and c) Fe $L_{2,3}$-edge energy loss spectra of $FeCl_3$-intercalated rGO. For these TEM analyses, GO thin film was deposited via five-cycle LbL assembly on a SiO_2/Si substrate followed by electrochemical reduction and $FeCl_3$ intercalation. Os coating was performed to protect the $FeCl_3$-rGO layer during the TEM specimen fabrication. d) C 1s and e) Fe $2p_{3/2}$ XPS spectra and f) Raman spectra of rGO and $FeCl_3$-intercalated rGO taken on three different positions for each sample. These samples were prepared on quartz substrates.

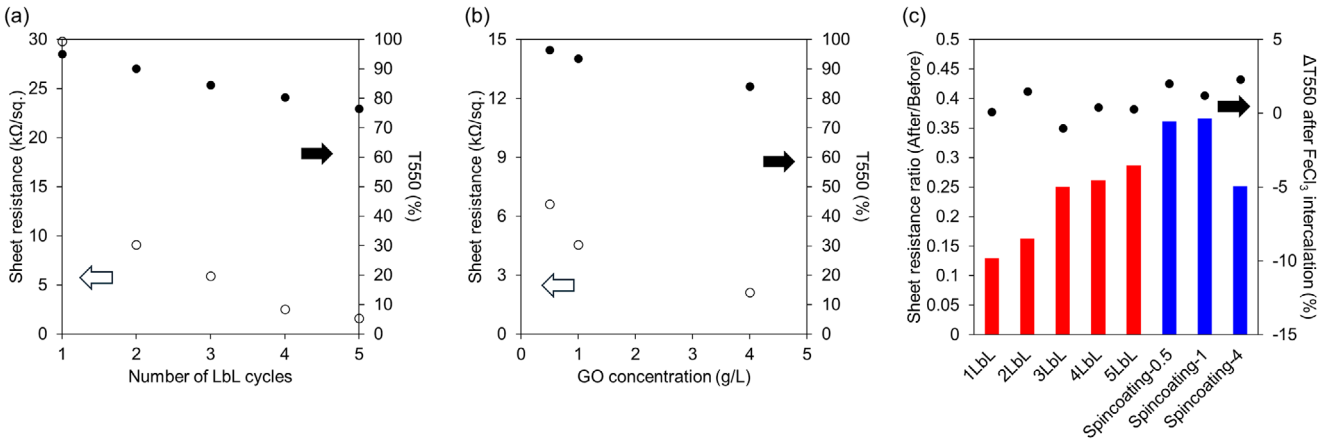

Figure 5. Sheet resistivity and optical transmittance at 550 nm (T550 (%)) plotted against a) LbL deposition cycles (1–5) and b) GO concentration used in spin coating (0.5–4 g L^{-1}). c) Reduction rates in resistivity due to $FeCl_3$ intercalation and T550 (%) for rGO TCFs prepared via LbL deposition and spin coating under different deposition conditions.

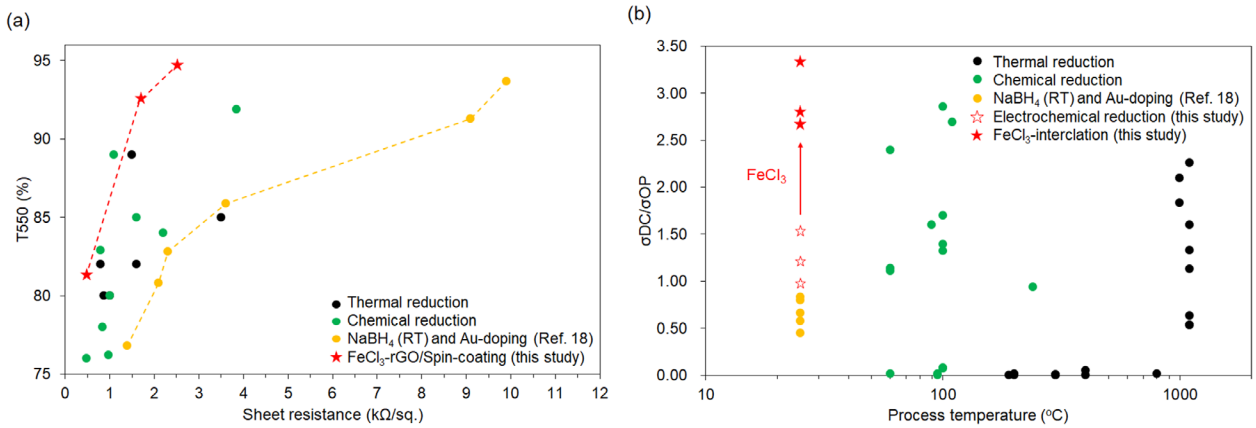

Figure 6. Comparison of GO-TCFs prepared by previously reported chemical and thermal reduction methods with GO-TCFs synthesized via electrochemical reduction and subsequent $FeCl_3$ intercalation in this study. a) Sheet resistance versus T550 (%). b) Process temperature versus $\sigma DC/\sigma OP$ for each method.

versus the number of deposition cycles revealed a linear relationship, indicating that the average film thickness was controlled according to the LbL deposition principle. Assuming a linear relationship between thickness and absorption, the estimated thicknesses of rGO films obtained from one, two, three, and four deposition cycles were 3, 7, 10, and 13 nm, based on the measured thickness of 15 nm for the rGO film prepared via five-cycle LbL deposition. A linear relationship was also observed between the number of deposition cycles and the resistivity of rGO-based TCFs fabricated using 2–5 LbL deposition cycles (1.6–9.1 $k\Omega\ sq^{-1}$). However, the film obtained after a single LbL deposition cycle exhibited higher resistance (29.8 $k\Omega\ sq^{-1}$), deviating from the linear trend. This deviation could be attributed to the incomplete coverage of the GO layer after the first LbL deposition cycle (Figure S5a, Supporting Information), which also likely associated with the particularly slow reduction rate observed during sample fabrication. To improve the quality of thin films with transmittances above 90%, a simple spin-coating method was developed. Similar to the LbL approach, the substrate surface was initially positively charged with PDDA modification. A GO dispersion was then deposited onto the substrate and spin-coated at 2,000 rpm. The rGO film formed following a single spin-coating attempt using a 1 g L^{-1} GO dispersion exhibited a transmittance of 94% at 550 nm, comparable to that of the film formed after a single LbL deposition cycle (95%) (Figure 5b). Scanning electron microscopy (SEM) observations revealed that the rGO film prepared via spin coating achieved nearly complete surface coverage (Figure S5b, Supporting Information). The film transmittance could be tuned by adjusting the dispersion concentration: A higher concentration of 4 g L^{-1} resulted in lower transmittance (84.1%), while a lower concentration of 0.5 g L^{-1} led to higher transmittance (96.4%). Notably, films with transmittance exceeding 90% exhibited improved resistivity, which should be attributed to the nearly uniform coverage of GO nanosheets on the substrate. The resistivity of the samples decreased by 60–80% following $FeCl_3$ intercalation. Meanwhile, the increase in transmittance at 550 nm was limited to ≈3% (Figure 5c). In general, the associated resistivity reduction rates were independent of the rGO film preparation conditions, highlighting the need for improved control over the $FeCl_3$ intercalation process. This optimization, along with a deeper investigation into the underlying mechanism, remains a key focus of our future research on chloride intercalation into rGO layers.

A literature review revealed that rGO-based TCFs prepared via electrochemical reduction and intercalation exhibit transparency/resistivity ratios superior to those achieved through chemical reduction and high-temperature thermal reduction processes (**Figure 6a**; Table S1, Supporting Information).[2,18,59–82] An estimated transmittance–resistivity boundary, derived from literature references, suggests that in the high-transmittance range (>90%), previously reported processes would likely struggle to achieve resistivity values comparable to those obtained in the present study. Compared to the previous room temperature process based on $NaBH_4$ reduction and subsequent Au^{3+} doping,[18] our electrochemical approach can produce much better TCFs. The relationship between processing temperatures and TCF performances was further discussed based on the figure of merit ($\sigma DC/\sigma OP$, with σDC and σOP denoting direct current conductivity and optical conductivity, respectively), calculated using Equation (3), as a function of process temperature for both the current study and previous methods (Table S1, Supporting Information).

$$\frac{\sigma DC}{\sigma OP} = \frac{Z_0}{2R\left(T^{-\frac{1}{2}} - 1\right)} \tag{3}$$

In this equation, Z_0 is the impedance of free space (377 Ω).[83] R is sheet resistance. T is transmittance of 550 nm. As shown in Figure 6b, the plots reveal that thermal reduction at ≈1000 °C is required to achieve high $\sigma DC/\sigma OP$ values. Chemical reduction still requires thermal activation at 60–100 °C. In contrast, electrochemical reduction at room temperature generally yields $\sigma DC/\sigma OP$ values comparable to those obtained through thermally accelerated chemical reduction, with a few exceptions. The plots also indicate that the electrochemical reduction–intercalation method achieves the highest $\sigma DC/\sigma OP$ value (3.5), underscoring the potential of the electrochemical route for serving as environmentally friendly processing techniques for rGO-based TCFs.

From this perspective, numerous opportunities are available for improving rGO-based TCF quality. First, the electrochemical reduction process is influenced by multiple factors, including solvent composition, electrolyte type and concentration, reduction bias, reaction time, and temperature. Our results revealed that using a non-aqueous electrolyte facilitates the formation of an extended π-electron network. Further regulation of the above parameters may yield more conductive rGO nanosheets by refining the reduction process. Although this study primarily focused on room-temperature processes, post-annealing at temperatures up to 500 °C is feasible for coatings on glass substrates. Under these circumstances, a thermochemically driven dehydration reaction between C—OH and C—H groups to promote C=C bond formation while minimizing CO_x evolution may be worth considering. Additionally, the considered temperature range enables the thermal intercalation of various metal chlorides, suggesting that identifying an optimal intercalant and intercalation conditions for rGO layers could further improve σDC/σOP in rGO-based TCFs. A systematic investigation of metal chloride intercalation into rGO is also expected to clarify how structural heterogeneities such as random stacking, carbon vacancies, and oxygen-containing functional groups influence intercalation kinetics and 2D molecular configurations within nanoscale interlayer spaces. These insights may result in the emergence of functionalities, including magnetic[84] and plasmonic[85] properties, that differ from those induced by intercalation into ideal graphene layers.

According to a recent review on state-of-the-art solution-processed TCFs for thin film solar cells,[86] a dip-coated carbon nanotube films exhibits a σDC/σOP of ≈35,[87] which may serve as a feasible next benchmark through the strategies outlined above. However, achieving σDC/σOP values comparable to those of TCFs based on CVD-grown graphene (≈100),[88] poly(3,4-ethylenedioxythiophene):polystyrene sulfonate (PEDOT:PSS) (≈120),[89] or silver nanowires (≈340)[90] remains a significant challenge. Therefore, it is still premature to position rGO thin films as candidates for high-end TCF applications. Nonetheless, their inherent advantages make them highly attractive to develop multifunctional thin film devices that require electromagnetic shielding, gas and moisture barrier performance, thermal management, or mechanical flexibility. The approach demonstrated in this study, which involves controlled reduction and active interlayer modification based on highly crystalline GO, is expected to provide a breakthrough toward improving the performance and applicability of rGO-based thin films beyond current limitations. Moreover, electrochemical reduction is applicable not only to thin films but also to GO-based bulk materials, porous structures, and composite assemblies.[49] Thus, the findings from this study, along with future research on process optimization and intercalation strategies, are expected to contribute to the advancement of a broad range of rGO-based nanomaterials.

Finally, from an industrial perspective, although the present study demonstrates the feasibility of tandem in-plane electrochemical reduction of GO and subsequent $FeCl_3$ intercalation using B-GO as a precursor, a more detailed mechanistic understanding would greatly benefit from the development of a quantitative kinetic model. Developing such a model would require systematic investigation of several key parameters that critically affect the reduction dynamics, including the size and geometry of the conductive support used to initiate in-plane reduction reactions, the configuration of the counter electrode, and the thickness of the GO film. Therefore, comprehensive future studies will be essential to fully elucidate the kitetic mechanism. In addtion, importantly, both the layer-by-layer (LbL) deposition and electrochemical processes employed in this study are compatible with roll-to-roll manufacturing techniques,[91,92] offering a pathway to cost-effective, large-scale production. Accordingly, the integration of these processes into roll-to-roll platforms represents a key objective toward the practical implementation of this technology.

3. Conclusion

This study demonstrated the feasibility of electrochemical rGO-based TCF fabrication through the controlled oxidation, reduction, and intercalation of GO. First, in-plane reduction of nanoscale GO thin films at room temperature was achieved using a highly crystalline B-GO precursor. The sharpening of the G and D bands in the Raman spectra after electrochemical reduction indicated that the resulting C—OH and C—H bonds prevented the introduction of local strain into the 2D lattice. This, in turn, facilitated the formation of an extended π-electron network. Subsequently, the resistivity of rGO-based TCFs was further reduced through electrochemical $FeCl_3$ intercalation, which induced hole doping. This finding demonstrates the potential of chloride intercalation chemistry to tailor the functionality of a wide range of rGO-based nanomaterials. Finally, the combination of these electrochemical methods helps surpass previous transparency/resistivity limitations for rGO-based TCFs.

4. Experimental Section

Synthesis of B-GO: B-GO was synthesized using a modified Brodie's method.[93] First, 1 g of graphite powder (FUJIFILM Wako Pure Chemical Corporation) was dispersed in 40 mL of fuming nitric acid (FUJIFILM Wako Pure Chemical Corporation) and stirred in an ice bath. Subsequently, 8 g of potassium chlorate (FUJIFILM Wako Pure Chemical Corporation) was gradually added, and the mixture was stirred at room temperature for 1 h. The resulting oxidized graphite was washed with pure water, collected via centrifugation at 3,000 rpm (Kubota; 3700), and dried in an oven at 50 °C. Next, 500 mg of oxidized graphite was dispersed in 500 mL of an ammonia solution (FUJIFILM Wako Pure Chemical Corporation) adjusted to pH 12.5. The dispersion was shaken for at least five days, following which it was transferred into 50 mL glass containers and subjected to ultrasonic treatment for 30 min to exfoliate graphite oxide into graphene oxide. Following centrifugation at 3,000 rpm, exfoliated flakes were removed, and the supernatant was collected at 8,000 rpm. Monolayer nanosheets were subsequently precipitated through high-speed centrifugation at 15,000 rpm. The precipitate was washed three times with pure water to obtain B-GO.

Synthesis of H-GO: H-GO was synthesized using a modified Hummers' method.[94] First, 2 g of graphite powder, 2 g of $NaNO_3$ (FUJIFILM Wako Pure Chemical Corporation), and 92 mL of concentrated sulfuric acid (FUJIFILM Wako Pure Chemical Corporation) were combined with 10 g of potassium permanganate (FUJIFILM Wako Pure Chemical Corporation), and the mixture was stirred in an ice bath. Subsequently, pure water was added gradually, followed by the addition of 5 mL of a hydrogen peroxide solution (FUJIFILM Wako Pure Chemical Corporation). After

centrifugation at 3,000 rpm and removal of the supernatant, the mixture was washed with a 5% HCl solution and pure water. The resulting oxidized graphite was dried in an oven maintained at 50 °C. The dried material was then dispersed in pure water at a 1:1 ratio and subjected to sonication for 2 h. The supernatant was collected by centrifugation at 8,000 rpm, while the precipitate was washed three times with pure water at 15,000 rpm to obtain H-GO.

Preparation of GO Thin Films—LbL Method: The substrates were treated with ultraviolet light and ozone (UV/ozone) prior to deposition to render their surface hydrophilic. First, the substrates were immersed in an aqueous solution of PDDA (100 g L^{-1}, pH = 9.1; FUJIFILM Wako Pure Chemical Corporation) for 5 min to create a positively charged surface with polycations. After rinsing with Milli-Q water and drying under an N_2 gas stream, the modified substrates were dipped into diluted GO solutions (6% (v/v) for B-GO and 6% (v/v) for H-GO, pH = 9.1) for 5 min, followed by the same rinsing and drying procedure. This alternating immersion process was repeated to achieve thin films with a controlled GO coating thickness.

Spin-Coating Method: As in the LbL method, the substrate was hydrophilized using ozone/UV treatment, immersed in the cationic solution for 5 min, rinsed with Milli-Q water, and dried under an N_2 gas stream. GO dispersions were then dropped onto the substrate to ensure complete coverage. Spin-coating was performed at 2,000 rpm for 12 s following a 5 min waiting period. Finally, the spin-coated film was rinsed with Milli-Q water and dried under an N_2 gas stream.

Electrochemical Reduction: GO thin films were electrochemically reduced using a three-electrode system comprising an Ag/AgCl reference electrode, a GC counter electrode, and a GO working electrode. After electrochemical reduction under a constant bias voltage, the samples were rinsed with Milli-Q water and dried under an N_2 gas stream.

Characterization: The morphology of GO nanosheets was analyzed using AFM (Nanocute; Hitachi High-Technologies Corporation). Elemental analysis was conducted using XPS (K-Alpha; Thermo Fisher Scientific). The C 1s XPS spectrum was deconvolved into three peaks: carbon bonds, C—O—C, and C—OH at 285.0, 286.4, and 287.1 eV, respectively. Cross-sectional TEM images of GO films were acquired using a JEM-ARM200F NEOARM (JEOL) at an acceleration voltage of 60 kV. The sheet resistance of the samples was measured using a Keithley 2450 source measurement unit. Measurements were taken at five points per sample, and the recorded values were averaged. The durability tests of $FeCl_3$–rGO TFCs were performed using a temperature-controlled incubator(SH-221; ESPEC). The transmittance spectra of rGO films were recorded using a Shimadzu SolidSpec-3700DUV. Raman spectra of the GO and rGO films were obtained using a laser confocal microscope (Raman microscopy, inVia Reflex, from Renishaw). A 100× objective lens was used to focus a 532 nm excitation laser on the sample surface. The Raman signals were detected using a CCD detection system (Andor) with an 1800 l mm^{-1} grating. The spatial resolution was horizontal 0.25 µm. The wavenumber resolution was 0.3 cm^{-1}. At least 3 different area was scanned for each substrate surface to examine the uniformity of the samples. The cells used for the in situ detection of CO_2 during the thermal, photo, and electrochemical reduction of GO films are illustrated in Figure S6 (Supporting Information). In this measurement system, a unidirectional flow of Ar carrier gas was maintained through a quartz cell at a rate of 12 ccm, carrying generated CO_2 from the GO film to the outlet, which was connected to a micro-GC detection system. For thermal reduction, a GO film was placed on a hot plate and heated to 230 °C. For photoinduced reduction, UV light from a mercury lamp was directed vertically onto the GO film, with the light source positioned 12 cm above the film. For electrochemical reduction, an electrochemical cell was installed within the gas detection cell. Additionally, CO_2 from rGO obtained via electrochemical reduction was monitored under UV irradiation.

Supporting Information

Supporting Information is available from the Wiley Online Library or from the author.

Acknowledgements

This work was partly supported by the World Premier International Research Center Initiative (WPI), MEXT, Japan, JSPS KAKENHI Grant Numbers 22K04875, 23KJ1771, 24K01304 Japan.

Conflict of Interest

The authors declare no conflict of interest.

Data Availability Statement

The data that support the findings of this study are available on request from the corresponding author. The data are not publicly available due to privacy or ethical restrictions.

Keywords

electrochemical reduction, graphene oxide, transparent conductive films

Received: April 25, 2025
Revised: June 16, 2025
Published online:

[1] Q. Zheng, W. Ip, X. Lin, N. Yousefi, K. Yeung, Z. Li, J. Kim, *ACS Nano* **2011**, *5*, 6039.
[2] X. Wang, L. Zhi, K. Müllen, *Nano Lett.* **2008**, *8*, 323.
[3] K. Novoselov, A. Geim, S. Morozov, D. Jiang, Y. Zhang, S. Dubonos, I. Grigorieva, A. Firsov, *Science* **2004**, *306*, 666.
[4] X. Li, G. Zhang, X. Bai, X. Sun, X. Wang, E. Wang, H. Dai, *Nat. Nanotechnol.* **2008**, *3*, 538.
[5] F. Bonaccorso, Z. Sun, T. Hasan, A. Ferrari, *Nat. Photonics* **2010**, *4*, 611.
[6] F. Liu, P. Li, H. An, P. Peng, B. McLean, F. Ding, *Adv. Funct. Mater.* **2022**, *32*, 2203191.
[7] A. Reina, X. Jia, J. Ho, D. Nezich, H. Son, V. Bulovic, M. Dresselhaus, J. Kong, *Nano Lett.* **2009**, *9*, 30.
[8] X. Li, W. Cai, L. Colombo, R. Ruoff, *Nano Lett.* **2009**, *9*, 4268.
[9] X. Li, W. Cai, J. An, S. Kim, J. Nah, D. Yang, R. Piner, A. Velamakanni, I. Jung, E. Tutuc, S. Banerjee, L. Colombo, R. Ruoff, *Science* **2009**, *324*, 1312.
[10] B. Deng, Z. Liu, H. Peng, *Adv. Mater.* **2019**, *31*, 1800996.
[11] J. Suk, A. Kitt, C. Magnuson, Y. Hao, S. Ahmed, J. An, A. Swan, B. Goldberg, R. Ruoff, *ACS Nano* **2011**, *5*, 6916.
[12] K. Kim, Y. Zhao, H. Jang, S. Lee, J. Kim, K. Kim, J. Ahn, P. Kim, J. Choi, B. Hong, *Nature* **2009**, *457*, 706.
[13] S. Stankovich, D. A. Dikin, R. D. Piner, K. A. Kohlhaas, A. Kleinhammes, Y. Jia, Y. Wu, S. T. Nguyen, R. S. Ruoff, *Carbon* **2007**, *45*, 1558.
[14] S. Pei, H.-M. Cheng, *Carbon* **2012**, *50*, 3210.
[15] S. Park, J. An, J. R. Potts, A. Velamakanni, S. Murali, R. S. Ruoff, *Carbon* **2011**, *49*, 3019.
[16] V. Agarwal, P. Zetterlund, *Chem. Eng. J.* **2021**, *405*, 127018.
[17] M. Agharkar, S. Kochrekar, S. Hidouri, M. Azeez, *Mater. Res. Bull.* **2014**, *59*, 323.
[18] H. J. Shin, K. K. Kim, A. Benayad, S. M. Yoon, H. K. Park, I. S. Jung, M. H. Jin, H. K. Jeong, J. M. Kim, J. Y. Choi, Y. H. Lee, *Adv. Funct. Mater.* **2009**, *19*, 1987.
[19] I. K. Moon, J. Lee, R. S. Ruoff, H. Lee, *Nat. Commun.* **2010**, *1*, 73.
[20] H. Feng, R. Cheng, X. Zhao, X. Duan, J. Li, *Nat. Commun.* **2013**, *4*, 1539.

[21] S. Yang, Q. Chen, M. Shi, Q. Zhang, S. Lan, T. Maimaiti, Q. Li, P. Ouyang, K. Tang, S. Yang, *Nanomaterials* **2020**, *10*, 770.
[22] A. Alayande, H. Park, J. Vrouwenvelder, I. Kim, *Small* **2019**, *15*, 1901023.
[23] V. Pham, H. Pham, T. Dang, S. Hur, E. Kim, B. Kong, S. Kim, J. Chung, *J. Mater. Chem.* **2012**, *22*, 10530.
[24] R. Larciprete, S. Fabris, T. Sun, P. Lacovig, A. Baraldi, S. Lizzit, *J. Am. Chem. Soc.* **2011**, *133*, 17315.
[25] R. Trusovas, K. Ratautas, G. Račiukaitis, J. Barkauskas, I. Stankevičienė, G. Niaura, R. Mažeikienė, *Carbon* **2013**, *52*, 574.
[26] L. Cheng, C. S. Yeung, L. Huang, G. Ye, J. Yan, W. Li, C. Yiu, F.-R. Chen, H. Shen, B. Z. Tang, Y. Ren, X. Yu, R. Ye, *Nat. Commun.* **2024**, *15*, 2925.
[27] M. Fatkullin, D. Cheshev, A. Averkiev, A. Gorbunova, G. Murastov, J. Liu, P. Postnikov, C. Cheng, R. D. Rodriguez, E. Sheremet, *Nat. Commun.* **2024**, *15*, 9711.
[28] D. Voiry, J. Yang, J. Kupferberg, R. Fullon, C. Lee, H. Y. Jeong, H. S. Shin, M. Chhowalla, *Science* **2016**, *353*, 1413.
[29] T. Miyata, S. Gohda, T. Fujii, H. Ono, H. Itoh, Y. Nishina, K. Kashimura, *Carbon* **2021**, *171*, 10.
[30] C. H. A. Wong, O. Jankovský, Z. Sofer, M. Pumera, *Carbon* **2014**, *77*, 508.
[31] T. Taniguchi, L. Nurdiwijayanto, N. Sakai, K. Tsukagoshi, T. Sasaki, T. Tsugawa, M. Koinuma, K. Hatakeyama, S. Ida, *Carbon* **2023**, *202*, 26.
[32] A. Bagri, C. Mattevi, M. Acik, Y. J. Chabal, M. Chhowalla, V. B. Shenoy, *Nat. Chem.* **2010**, *2*, 581.
[33] S. Pei, Q. Wei, K. Huang, H.-M. Cheng, W. Ren, *Nat. Commun.* **2018**, *9*, 145.
[34] J. Guo, S. Pei, K. Huang, Q. Zhang, X. Zhou, J. Tong, Z. Liu, H.-M. Cheng, W. Ren, *Nat. Commun.* **2025**, *16*, 727.
[35] B. Gurzęda, N. Boulanger, M. R. V. Jørgensen, I. Kantor, A. V. Talyzin, *Carbon* **2024**, *221*, 118899.
[36] J.-C. Yoon, X. Dai, K.-N. Kang, J. Hwang, M.-J. Kwak, F. Ding, J.-H. Jang, *ACS Nano* **2021**, *15*, 11655.
[37] M. Hada, K. Miyata, S. Ohmura, Y. Arashida, K. Ichiyanagi, I. Katayama, T. Suzuki, W. Chen, S. Mizote, T. Sawa, T. Yokoya, T. Seki, J. Matsuo, T. Tokunaga, C. Itoh, K. Tsuruta, R. Fukaya, S. Nozawa, S.-I. Adachi, J. Takeda, K. Onda, S.-Y. Koshihara, Y. Hayashi, Y. Nishina, *ACS Nano* **2019**, *13*, 10103.
[38] T. Taniguchi, S. Kurihara, H. Tateishi, K. Hatakeyama, M. Koinuma, H. Yokoi, M. Hara, H. Ishikawa, Y. Matsumoto, *Carbon* **2015**, *84*, 560.
[39] T. Taniguchi, H. Yokoi, M. Nagamine, H. Tateishi, A. Funatsu, K. Hatakeyama, C. Ogata, M. Ichida, H. Ando, M. Koinuma, Y. Matsumoto, *J. Phys. Chem. C* **2014**, *118*, 28258.
[40] H. Otsuka, K. Urita, N. Honma, T. Kimuro, Y. Amako, R. Kukobat, T. J. Bandosz, J. Ukai, I. Moriguchi, K. Kaneko, *Nat. Commun.* **2024**, *15*, 1708.
[41] A. Nordenström, A. Iakunkov, N. Boulanger, G. Li, C. Hennig, I. Baburin, M. Jørgensen, I. Kantor, A. V. Talyzin, *Carbon* **2023**, *203*, 770.
[42] T. Taniguchi, K. C. Wong, L. Nurdiwijayanto, K. Hatakeyama, K. Awaya, S. Ida, M. Koinuma, S. Ueda, M. Osada, H. Yokoi, *Carbon* **2021**, *177*, 26.
[43] K. Erickson, R. Erni, Z. Lee, N. Alem, W. Gannett, A. Zettl, *Adv. Mater.* **2010**, *22*, 4467.
[44] T. Tsugawa, K. Hatakeyama, M. Koinuma, N. Moriyama, S. Ida, *Small* **2024**, *20*, 2400707.
[45] D. Zhan, L. Sun, Z. H. Ni, L. Liu, X. F. Fan, Y. Wang, T. Yu, Y. M. Lam, W. Huang, Z. X. Shen, *Adv. Funct. Mater.* **2010**, *20*, 3504.
[46] W. Zhao, P. H. Tan, J. Liu, A. C. Ferrari, *J. Am. Chem. Soc.* **2011**, *133*, 5941.
[47] H. Kinoshita, I. Jeon, M. Maruyama, K. Kawahara, Y. Terao, D. Ding, R. Matsumoto, Y. Matsuo, S. Okada, H. Ago, *Adv. Mater.* **2017**, *29*, 1702141.
[48] M. Zhou, Y. Wang, Y. Zhai, J. Zhai, W. Ren, F. Wang, S. Dong, *Chem.-Eur. J.* **2009**, *15*, 6116.
[49] X. Feng, W. Chen, L. Yan, *RSC Adv.* **2016**, *6*, 80106.
[50] Y. Yoon, H. Kye, W. Yang, J. Kang, *Appl. Sci.* **2020**, *10*, 2015.
[51] J. A. Quezada-Renteria, C. O. Ania, L. F. Chazaro-Ruiz, J. R. Rangel-Mendez, *Carbon* **2019**, *149*, 722.
[52] T. Taniguchi, L. Nurdiwijayanto, R. Ma, T. Sasaki, *Appl. Phys. Rev.* **2022**, *9*, 021313.
[53] J. L. Hart, K. Hantanasirisakul, A. C. Lang, B. Anasori, D. Pinto, Y. Pivak, J. T. van Omme, S. J. May, Y. Gogotsi, M. L. Taheri, *Nat. Commun.* **2019**, *10*, 522.
[54] F. Kang, Y. Leng, T.-Y. Zhang, B. Li, *Carbon* **1998**, *36*, 383.
[55] D. J. Wehenkel, T. H. Bointon, T. Booth, P. Boggild, M. F. Craciun, S. Russo, *Sci. Rep.* **2015**, *5*, 7609.
[56] A. Nyrow, C. Sternemann, J. S. Tse, C. Weis, C. J. Sahle, K. Mende, D. C. F. Wieland, V. Cerantola, R. A. Gordon, G. Spiekermann, T. Regier, M. Wilke, M. Tolan, *J. Anal. At. Spectrom.* **2016**, *31*, 815.
[57] J. Liu, Q. Li, Y. Zou, Q. Qian, Y. Jin, G. Li, K. Jiang, S. Fan, *Nano Lett.* **2013**, *13*, 6170.
[58] K. K. Walsh, C. Murphy, G. Jones, M. Barnes, A. D. Santis, D. W. Shin, S. Russo, M. Craciun, *Photon. Sol. Energy Syst. VII* **2018**, *8*, 10688.
[59] J. Geng, L. Liu, S. Yang, S. Youn, D. Kim, J. Lee, J. Choi, H. Jung, *J. Phys Chem. C* **2010**, *114*, 14433.
[60] F. Oytun, F. Basarir, *Mater. Lett.* **2019**, *257*, 126756.
[61] M. Saychak, N. Borodinov, R. Burtovyy, M. Anayee, K. Hu, R. Ma, A. Grant, H. Li, D. Cutshall, Y. Wen, G. Koley, W. Harrell, G. Chumanov, V. Tsukruk, I. Luzinov, *ACS Appl. Mater. Interfaces* **2018**, *10*, 3975.
[62] H. He, X. Li, J. Wang, T. Qiu, Y. Fang, Q. Song, B. Luo, X. Zhang, L. Zhi, *Small* **2013**, *9*, 820.
[63] H. Becerril, J. Mao, Z. Liu, R. Stoltenberg, Z. Bao, Y. Chen, *ACS Nano* **2008**, *2*, 463.
[64] J. Wu, M. Agrawal, H. Becerril, Z. Bao, Z. Liu, Y. Chen, P. Peumans, *ACS Nano* **2010**, *4*, 43.
[65] C. Mattevi, G. Eda, S. Agnoli, S. Miller, K. Mkhoyan, O. Celik, D. Mastrogiovanni, G. Granozzi, E. Garfunkel, M. Chhowalla, *Adv. Funct. Mater.* **2009**, *19*, 2577.
[66] G. Eda, G. Fanchini, M. Chhowalla, *Nat. Nanotechnol.* **2008**, *3*, 270.
[67] Q. Zheng, M. Gudarzi, S. Wang, Y. Geng, Z. Li, J. Kim, *Carbon* **2011**, *49*, 2905.
[68] J. Miao, H. Liu, C. Li, X. Zhang, *Sci. Adv. Mater.* **2016**, *8*, 1066.
[69] H. Shi, C. Wang, Z. Sun, Y. Zhou, K. Jin, G. Yang, *Sci. China Phys. Mech.* **2015**, *58*, 1.
[70] D. Konios, C. Petridis, G. Kakavelakis, M. Sygletou, K. Savva, E. Stratakis, E. Kymakis, *Adv. Funct. Mater.* **2015**, *25*, 2213.
[71] J. Zhao, S. Pei, W. Ren, L. Gao, H. Cheng, *ACS Nano* **2010**, *4*, 5245.
[72] S. Pei, J. Zhao, J. Du, W. Ren, H. Cheng, *Carbon* **2010**, *48*, 4466.
[73] F. Yao, W. Li, S. Karthikeyan, C. Fukuhara, S. Badhulika, C. Kong, *Chem. Eng. J.* **2024**, *488*, 150828.
[74] X. Li, D. Zhang, C. Yang, Y. Shang, *J. Nanosci. Nanotechnol.* **2015**, *15*, 9500.
[75] S. Jo, H. Moon, Y. Kim, H. Dow, J. Lee, *J. Korean Inst. Met. Mater.* **2022**, *60*, 570.
[76] T. Fan, C. Yuan, W. Tang, S. Tong, Y. Liu, W. Huang, Y. Min, A. Epstein, *Chin. Phys. Lett.* **2015**, *32*, 076802.
[77] J. Ning, L. Hao, M. Jin, X. Qiu, Y. Shen, J. Liang, X. Zhang, B. Wang, X. Li, L. Zhi, *Adv. Mater.* **2017**, *29*, 1605028.
[78] S. Domingues, I. Kholmanov, T. Kim, J. Kim, C. Tan, H. Chou, Z. Alieva, R. Piner, A. Zarbin, R. Ruoff, *Carbon* **2013**, *63*, 454.
[79] S. Mihara, T. Tsubota, N. Murakami, T. Ohno, *J. Nanosci. Nanotechnol.* **2012**, *12*, 6930.
[80] R. Karthick, M. Brindha, M. Selvaraj, S. Ramu, *J. Colloid Interface Sci.* **2013**, *406*, 69.
[81] D. Li, M. Müller, S. Gilje, R. Kaner, G. Wallace, *Nat. Nanotechnol.* **2008**, *3*, 101.
[82] V. Pham, T. Cuong, S. Hur, E. Shin, J. Kim, J. Chung, E. Kim, *Carbon* **2010**, *48*, 1945.

[83] Q. Zheng, Z. Li, J. Yang, J. Kim, *Prog. Mater. Sci.* **2014**, *64*, 200.
[84] T. H. Bointon, I. Khrapach, R. Yakimova, A. V. Shytov, M. F. Craciun, S. Russo, *Nano Lett.* **2014**, *14*, 1751.
[85] F. J. Bezares, A. D. Sanctis, J. R. M. Saavedra, A. Woessner, P. A. Gonzalez, I. Amenabar, J. Chen, T. H. Bointon, S. Dai, M. M. Fogler, D. N. Basov, R. Hillenbrand, M. F. Craciun, F. J. G. Abajo, S. Russo, F. H. L. Koppens, *Nano Lett.* **2017**, *17*, 5908.
[86] Y. Zhang, S. W. Ng, X. Lu, Z. Zheng, *Chem. Rev.* **2020**, *120*, 2049.
[87] F. Mirri, A. W. K. Ma, T. T. Hsu, N. Behabtu, S. L. Eichmann, C. C. Young, D. E. Tsentalovich, M. Pasquali, *ACS Nano* **2012**, *6*, 9737.
[88] S. Bae, H. Kim, Y. Lee, X. Xu, J. S. Park, Y. Zheng, J. Balakrishnan, T. Lei, H. R. Kim, Y. I. Song, Y. J. Kim, K. S. Kim, B. Ozyilmaz, J. H. Ahn, B. H. Hong, S. Iijima, *Nat. Nanotechnol.* **2010**, *5*, 574.
[89] X. Hu, X. Meng, L. Zhang, Y. Zhang, Z. Cai, Z. Huang, M. Su, Y. Wang, M. Li, F. Li, X. Yao, F. Wang, W. Ma, Y. Chen, Y. Song, *Joule* **2019**, *3*, 2205.
[90] L. J. Andres, M. F. Menendez, D. Gomez, A. L. Martinez, N. Bristow, J. P. Kettle, A. Menendez, B. Ruiz, *Nanotechnol.* **2015**, *26*, 265201.
[91] B. Deng, R. Xu, X. Wang, L. An, K. Zhao, G. J. Cheng, *Energy Storage Mater.* **2019**, *22*, 450.
[92] B. D. L. Campeon, M. Akada, M. S. Ahmad, Y. Nishikawa, K. Gotoh, Y. Nishina, *Carbon* **2020**, *158*, 356.
[93] T. Tsugawa, K. Hatakeyama, J. Matsuda, M. Koinuma, S. Ida, *Bull. Chem. Soc. Jpn.* **2021**, *94*, 2195.
[94] K. Hatakeyama, M. Koinuma, Y. Shimizu, Y. Hakuta, *Bull. Chem. Soc. Jpn.* **2019**, *92*, 511.